



Research paper

Hydrodynamics and secondary currents in an asymmetrical rectangular canal with streamwise beam

PEDRO X. SANCHEZ, Undergraduate Student, *School of Civil Engineering, The University of Queensland, Brisbane, Australia*
Email: pedro.sanchezmichilena@uq.net.au

XINQIAN LENG , Research Fellow, *School of Civil Engineering, The University of Queensland, Brisbane, Australia*
Email: xinqian.leng@uqconnect.edu.au

HUBERT CHANSON  (IAHR Member), *School of Civil Engineering, The University of Queensland, Brisbane, Australia*
Email: h.chanson@uq.edu.au (author for correspondence)

ABSTRACT

While the literature on transverse beams in open channels is broad, there is comparatively less understanding of the hydrodynamics of channels with streamwise ribs. In the current study, an asymmetrical canal with a sidewall longitudinal beam was studied experimentally to gain some fundamental understanding of the implications in terms of turbulence and environmental applications. The sidewall beam induced regular losses along the canal, with a complicated velocity field and secondary currents. The data showed a contrasted longitudinal velocity map, with high and low velocity zones. The lowest velocities were typically recorded underneath the sidewall beam. Complicated secondary currents of Prandtl's second kind developed in the inner and outer corners of the beams, as well as in the square cavity underneath.

Keywords: Asymmetrical rectangular flume; open channel hydrodynamics; physical modelling; secondary currents; sidewall streamwise rib

1 Introduction

Although the literature on transverse rib/vane/beam is very extensive in mechanical, aeronautical, chemical, civil and environmental engineering (e.g. Adachi, 1964; Djenidi, Elavarasan, & Antonia, 1999; Knight & Macdonald, 1979; Morris, 1955), channels with longitudinal beams have been less studied, albeit the idea is not novel. Streamwise beams along channel walls have been successfully tested for the increased heat transfer rate (Chang, Lin, & Liou, 2008; Naik, Probert, & Bryden, 1999) and mass transfer in chemical engineering (Stamou, 2008). The longitudinal ribs increase the wetted perimeter and the surface contact area with the fluid. A related design was developed for biological filtration (Roo, 1965). Longitudinal beams are used in a number of stages of water treatment plants, e.g. maze flocculators, high-rate clarification tube settlers, sedimentation basins with plate settlers and sludge clarifiers (Degremont, 1979; Randtke & Horsley, 2012). In settling tank and

sediment basin decant systems, longitudinal vanes are designed to minimize large-scale turbulence and to maximize the settling processes. Similar designs are also used on stormwater treatment systems and combined sewers (FNDAE, 1988). In turbulent boundary layers, longitudinal ribs and their configuration have a major impact on secondary flow motion, as well as tertiary and quaternary flows (Hwang & Lee, 2018). The existence of large secondary vortical structures is closely linked to the relative spanwise spacing of the beams (Vanderwel & Ganapathisubramani, 2015).

The purpose of the present hydrodynamic investigation is to characterize the role of an asymmetrical streamwise beam on the flow field in a rectangular channel, like a box culvert barrel. The aim is to gain some fundamental understanding of the turbulence modifications and implications in terms of environmental applications, e.g. mass transfer and fish passage. This study is based upon some detailed physical modelling under controlled conditions.

Received 11 April 2019; accepted 6 January 2020/Open for discussion until 1 September 2021.

2 Physical facility and experiments

2.1 Dimensional considerations

Considering the simplistic case of a steady turbulent flow in a rectangular asymmetrical channel with a streamwise beam sketched in Fig. 1, a dimensional analysis gives a series of dimensionless relationships between the steady flow field at a location (x, y, z) and the inflow conditions, channel characteristics, and fluid and physical properties:

$$\begin{pmatrix} \frac{d}{d_c}, \\ \frac{V_x}{V_c}, \\ \frac{v_x'}{V_c}, \\ \frac{P}{\rho g d_c}, \\ \frac{\tau_o}{\rho g d_c}, \dots \end{pmatrix} = F \left(\begin{pmatrix} \frac{x}{d_c}, \frac{y}{d_c}, \frac{z}{d_c}, \\ \frac{B}{d_c}, \theta, \frac{k_s}{d_c}, \frac{Z_R}{d_c}, \frac{h_R}{d_c}, \frac{l_R}{d_c}, \frac{r_R}{d_c}, \\ \frac{d_1}{d_c}, \frac{V_1}{\sqrt{g d_1}}, \frac{v_1'}{V_1}, \\ \frac{VD_H}{\mu}, \frac{g \mu^4}{\rho \sigma^3}, \dots \end{pmatrix} \right) \quad (1)$$

where d is the flow depth, V_x is the longitudinal velocity component, v_x' is the velocity fluctuation, P is the local pressure, τ_o is the boundary shear stress, d_c the critical flow depth, V_c the critical flow velocity, x, y and z are respectively the longitudinal, transverse and vertical coordinates, B is the channel width, θ is the angle between the bed and horizontal, Z_R is the elevation of the rib bottom above the channel bed, h_R is the height of the rib, l_R is the rib breadth, r_R is the radius of curvature of the rib edges (Fig. 1), d_1 is the inflow depth, V_1 and v_1' are the inflow velocity and velocity fluctuation respectively, D_H is the hydraulic diameter, ρ is the water density, μ is the water dynamic viscosity, σ is the surface tension, and g is the gravity acceleration. Note the introduction of the critical flow depth and velocity in Eq. (1) as the relevant length and velocity scales. This approach is common in free-surface flow studies when a Froude similarity is applied. In the right hand side of Eq. (1), the 12th, 14th and 15th terms are respectively the inflow Froude number, the Reynolds number R_e and Morton number. Since most open channel flow studies are undertaken with air and water in both geometrically-scaled channel and prototype structure, the Morton number becomes an invariant in Eq. (1).

Considering the flow in an asymmetrical rectangular channel (Fig. 1), the above analysis shows a large number of relevant parameters. Any true similarity would require identical dimensionless variables, including Froude, Reynolds and Morton numbers, in both laboratory and at full-scale. This is physically impossible in view of the large number of independent parameters in Eq. (1) (right hand side). In the present study, the physical modelling was based upon a Froude similarity and the laboratory experiments were conducted in a relatively large-size facility operating at relatively large Reynolds numbers: $0.6 \times 10^5 < R_e < 2.5 \times 10^5$.

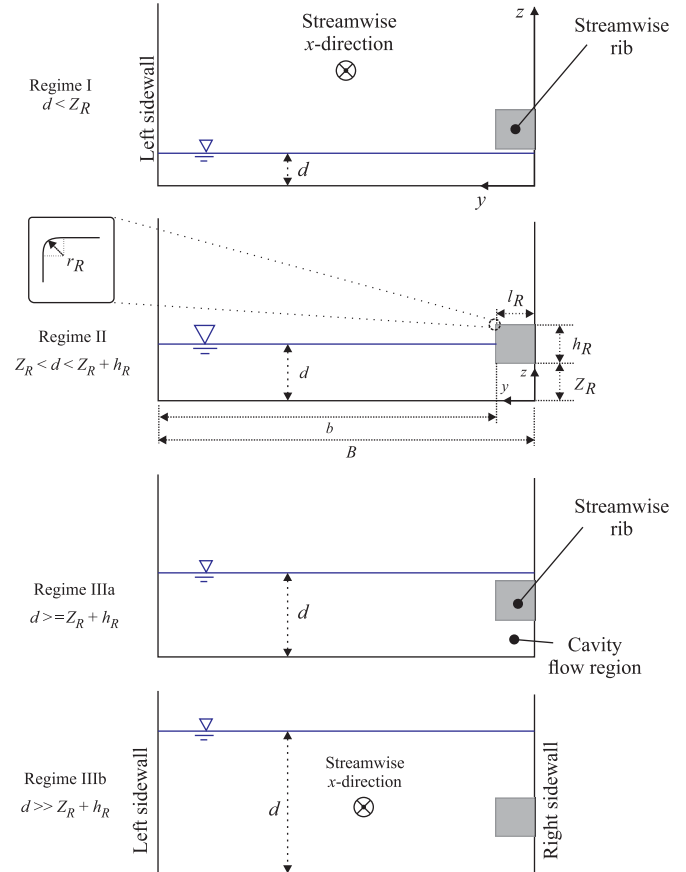


Figure 1 Definition sketch of flow regimes in an asymmetrical rectangular channel with a streamwise beam – looking downstream for the present configuration

2.2 Experimental facility and instrumentation

The experiments were conducted in a 15 m long and 0.5 m wide ($B = 0.50$ m) tilting flume. The bed and sidewalls of the flume were made of PVC and glass respectively. The bed of the channel was horizontal, i.e. $S_o = \sin\theta = 0$ for all experiments, thus simplifying Eq. (1). Upstream of the flume, the water was supplied by a 2 m long 1.25 m wide intake structure, fed by a constant head tank, and equipped with baffles, flow straighteners leading to a three-dimensional convergent, ensuring smooth inflow conditions at the flume's upstream end. At the downstream end, the flume ended with a free overfall.

A 12 m long square rib ($h_R = l_R = 0.050$ m) was installed along the right sidewall (Fig. 1). The square profile had sharp edges: $r_R \approx 0$ (Sanchez, Leng, & Chanson, 2018). The rib was made of smooth acrylic and it was installed at $Z_R = 0.050$ m above the bed, based upon Watson, Goodrich, Cramp, Gordos, and Franklin (2018), with an accuracy of ± 1 mm over its full length. The longitudinal rib was located between $x = 1$ m and 13 m, where x is the longitudinal distance from the inlet of the flume and positive downstream.

The water discharge was measured using a Venturi meter installed in the supply line, designed based upon British Standard (1943). The percentage error of the flow rate was estimated to be less than 2%. A rail-mounted pointer gauge was used

to measure the free surface elevation with an accuracy of ± 0.5 mm. Three velocimeter systems were used. A Prandtl–Pitot tube was used to measure the velocity and pressure in the water flow. The Pitot tube was a Dwyer® 166 Series Prandtl–Pitot tube with a $\varnothing 3.18$ mm tube made of corrosion resistant stainless steel, a hemispherical total pressure tapping ($\varnothing = 1.19$ mm) at the tip and four equally spaced static pressure tappings ($\varnothing = 0.51$ mm) located 25.4 mm behind the tip. Further velocity measurements were performed with a roving Preston tube (RPT) type C1.6(r) (Macintosh, 1990). The RPT comprised two stainless steel pressure tubes: a dynamic pressure tube (1.62 mm OD) with 20 mm upstream projection; and a wake pressure tube (1.62 mm OD) directed normal to the boundary surface with a 1 mm clearance. Both the Prandtl–Pitot tube and RPT were connected to 30° inclined manometers, with the manometer tubes opened to the atmosphere. Additional velocity measurements were performed with an acoustic Doppler velocimeter (ADV) Nortek™ Vectrino+ equipped with a three-dimensional side-looking head. The data were collected by setting a sampling rate of 200 Hz for 180 s at each point. The velocity range was ± 1 m s⁻¹, the transmit length was 0.3 mm and the control volume was 1 mm. The ADV signal data were post-processed using the software WinADV. Erroneous data with an average correlation of less than 60% and an average SNR less than 5 dB were removed. In addition, the signal was “despiked” using a phase-space thresholding technique (Chanson, Trevethan, & Aoki, 2008; Goring & Nikora, 2002; Wahl, 2003). The percentage of good ADV samples was larger than 45% for all data, ensuring a minimum of 16,200 good samples at each sampling point. The vertical translation of the velocimeter was controlled by a fine adjustment travelling mechanism connected to a digital scale unit. The error on the vertical position of the probes was $\Delta z < \pm 0.025$ mm. The accuracy on the longitudinal position was estimated as $\Delta x < \pm 2$ mm. The accuracy on the transverse position of the probes was about ± 1 mm. The experiments were documented with a dSLR camera Pentax™ K-3 and a digital camera Casio™ Exilim EX-10.

The Prandtl–Pitot tube and RPT were used to determine the local boundary shear stress, i.e. the skin friction, in a turbulent channel flow, when the tube is in contact with the wall (Macintosh, 1990; Patel, 1965; Preston, 1954). Their respective calibration showed a monotonic relationship between measured velocity and boundary shear stress (Sanchez et al., 2018).

3 Basic flow patterns

3.1 Presentation

Flow patterns were observed for unit discharges ranging from 0.016 m² s⁻¹ to 0.20 m² s⁻¹. For all flow rates, the water depth was larger than the critical flow depth (Appendix 1). The free-surface profile corresponded to a H2 backwater profile for all flow conditions and flow regimes. The visual observations showed four main flow patterns, sketched in Fig. 1.

Regime I was simply a gradually-varied flow in a rectangular symmetrical channel. The longitudinal rib had no effect on the flow and this was observed for $q < 0.024$ m² s⁻¹. Regime II was recorded for 0.024 m² s⁻¹ $< q < 0.070$ m² s⁻¹. The sidewall rib interacted with the upper flow region and the free-surface width was narrower: $b = B - l_R$ (Fig. 1). Visual observations and dye injection showed that the rib presence shifted the high-velocity flow region towards the smooth vertical left sidewall. Beneath the rib, i.e. $y < l_R$ and $z < Z_R$, the fluid motion in the square cavity tended to be dominated by a secondary motion with an elongated longitudinal large-scale eddy. Dye injection indicated limited mixing between the cavity flow and main flow.

For $q \geq 0.070$ m² s⁻¹ and $d \geq (Z_R + h_R)$ (Regime IIIa), the free-surface interacted with the upper face of the rib next to the right sidewall. The fluid flow above the rib, i.e. $y < l_B$ and $z > Z_R + h_R$, was affected by boundary friction and corner flows, forming an upper low velocity region. Overall, the rib tended to shift the main flow, in particular the high-velocity zones, towards the left sidewall. At larger discharges, i.e. $d \gg (Z_R + h_R)$ (Regime IIIb), the main flow was less affected by the sidewall rib. The fluid flow in the square cavity beneath the right sidewall rib was however slower than the main flow. Dye injection observations showed little mixing between the main flow and the cavity region, with relatively long-lasting turbulent eddies in the square cavity below the beam.

Free surface measurements were conducted to document the total flow resistance of the channel in presence of the streamwise beam (Section 3.2). Free surface measurements were further conducted in a 12 m long 0.5 m wide smooth horizontal channel (without rib). The comparative data showed a similar free-surface pattern between both configurations, albeit with an increase of around 10% in water depth in presence of the sidewall beam for an identical water discharge.

3.2 Flow resistance

The flow resistance of the streamwise beam channel was derived from the measured free-surface profile and slope of the total head line. The latter was related to the Darcy–Weisbach friction factor f , which is a dimensionless expression of the average boundary shear stress in the channel (Liggett, 1994; Montes, 1998). The data are reported in Table 1 and Fig. 2. For practical reasons, the Chézy coefficient $C_{Chézy}$ and Gauckler–Manning coefficient n_{GM} are also reported in Table 1, based upon flow properties recorded at $x = 8$ m.

The flow resistance in the ribbed channel was greater than that in a smooth rectangular channel for the same flow conditions (Fig. 2). For example, with a Reynolds number of 50,000, the friction factor of the ribbed channel was nearly twice the friction factor for a smooth turbulent flow. The increased flow resistance was likely caused by strong secondary current motion, local discontinuity and intense turbulence induced

Table 1 Flow resistance coefficients for the asymmetrical sidewall beam channel

Q	Regime	$d^{(1)}$	$D_H^{(1)}$	Re	f	$C_{Chézy}$	n_{GM}
($m^3 s^{-1}$)		(m)	(m)			($m^{1/2} s^{-1}$)	($s m^{-1/3}$)
0.008	I	0.0495	0.165	4.9×10^4	0.0405	44.0	0.0134
0.015	II	0.069	0.170	8.6×10^4	0.0318	49.7	0.0119
0.0261	II	0.0925	0.211	1.4×10^4	0.0248	56.3	0.0109
0.035	II–III	0.1115	0.244	1.7×10^4	0.0230	58.4	0.0107
0.0556	III	0.1475	0.302	2.5×10^4	0.0205	61.8	0.0105
0.100	III	0.2075	0.380	3.9×10^4	0.0148	72.9	0.0093

Note: ⁽¹⁾ measurements at $x = 8$ m.

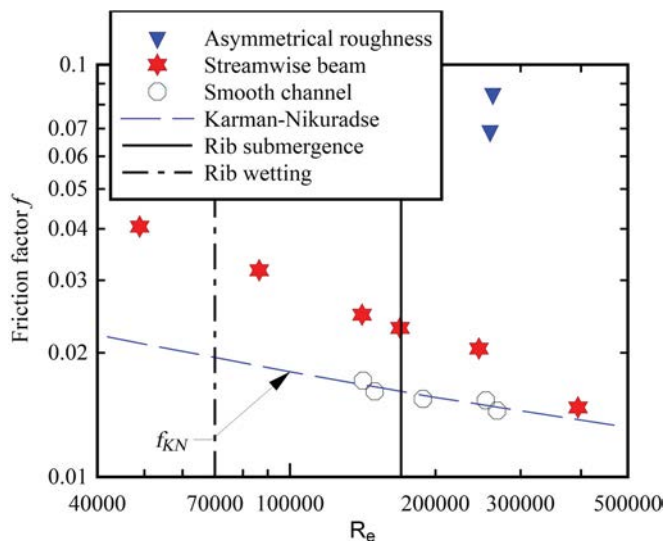


Figure 2 Darcy-Weisbach friction factor f for the streamwise rib channel as a function of the Reynolds number Re – comparison with the Karman–Nikuradse formula for smooth turbulent flow, smooth open channel flow data and asymmetrical roughened channel data (Wang et al., 2018) – the rib wetting and rib submergence are highlighted with vertical lines

by the rib presence. The associated turbulent dissipation contributed to both total head losses and flow resistance. With the streamwise beam, the channel flow resistance was best correlated by:

$$f = f_{KN} + 0.02775 \exp\left(-\frac{Re}{8.09 \times 10^6}\right) \quad (2)$$

where Re is the Reynolds defined in terms of the hydraulic diameter (Eq. 1) and f_{KN} is the smooth turbulent flow friction factor predicted based upon the Karman–Nikuradse formula (Rouse 1938; Schlichting, 1979). The present data, as well as Eq. (2), implied a trend for which the presence of the sidewall beam would tend to have a lesser effect on the flow resistance at large discharges and large Reynolds numbers. Indeed, in Regime IIIb, the relative impact of the beam on the cross-sectional shape and wetted perimeter becomes increasingly smaller and smaller with increasing flow rates. Figure 2 includes also a comparison in terms of flow resistance between

the asymmetrical ribbed channel and a channel with asymmetrical boundary roughness. The friction factor for the longitudinal rib channel was lower than that in the asymmetrical rough surface configurations (Fig. 2).

Overall, the asymmetrical beam channel configuration seemed to moderately affect the flow resistance, when compared to other methods (e.g. asymmetrical roughening) used to create low-velocity zones, for example to facilitate biofilm development and enhance contaminant dilution.

4 Turbulent velocity results

4.1 Presentation

The Prandtl–Pitot tube data provided vertical distributions of pressures. At all measurement locations, the results showed that the pressure was hydrostatic everywhere. The time-averaged velocity data are presented in this section.

In the presence of the sidewall beam, the longitudinal velocity data showed a consistent pattern. For $z > Z_R + h_R$, large velocities were observed about the centreline of the flume as illustrated in Figs 3 and 4. At lower vertical elevations, the maximum longitudinal velocities tended to shift away from the ribbed sidewall, towards $0.4 < y/B < 0.7$ (Figs 4 and 5). For example, about $0.2 \text{ m} < y < 0.35 \text{ m}$ in Fig. 4a and b. A similar pattern was reported in open channel flows with asymmetrical roughness (Cabonice, Fernando, Wang, & Chanson, 2019; Tomimaga & Nezu, 1991; Wang, Uys, & Chanson, 2018). All these experiments were performed in flumes of comparable length and width (Table 2). Typical vertical distributions and contour plots of longitudinal velocity are presented in Figs 3 and 4. In Fig. 3, the blue line represents the water surface. The velocity distributions showed a three-dimensional, asymmetrical and fully-developed flow, owing to the longitudinal rib presence. A typical centreline velocity profile is plotted in Fig. 3b, in which the data are compared with the theoretical log-wake law velocity distribution (Chanson, 2014; Schlichting, 1979). Overall, there was a close agreement between the physical data and theory on the channel centreline. The velocity data followed the no-slip boundary condition at the solid boundaries. All the data showed a low velocity region located underneath the sidewall

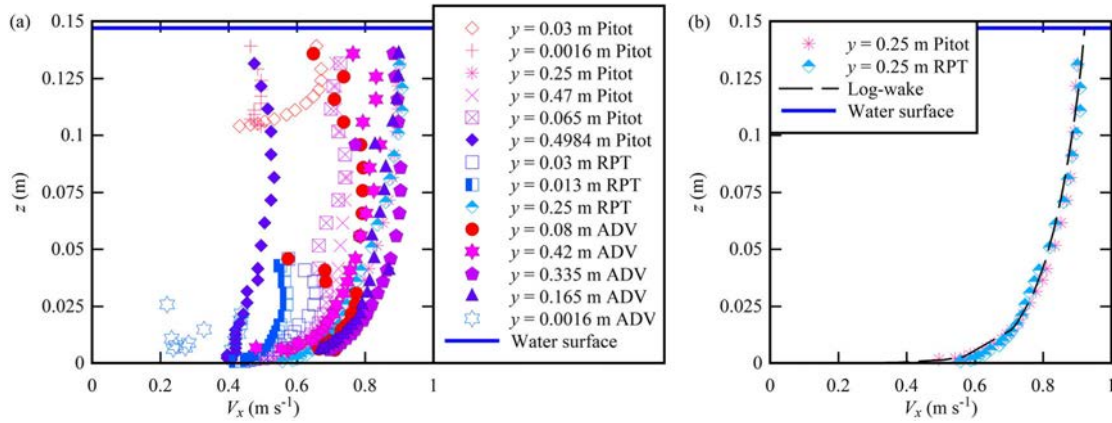


Figure 3 Vertical profiles of longitudinal velocity component V_x (m s⁻¹) in the streamwise ribbed channel – flow conditions: $Q = 0.0556$ m³ s⁻¹, $x = 8$ m, $d = 0.147$ m. (a) All data; (b) centreline vertical profiles compared to the log-wake law

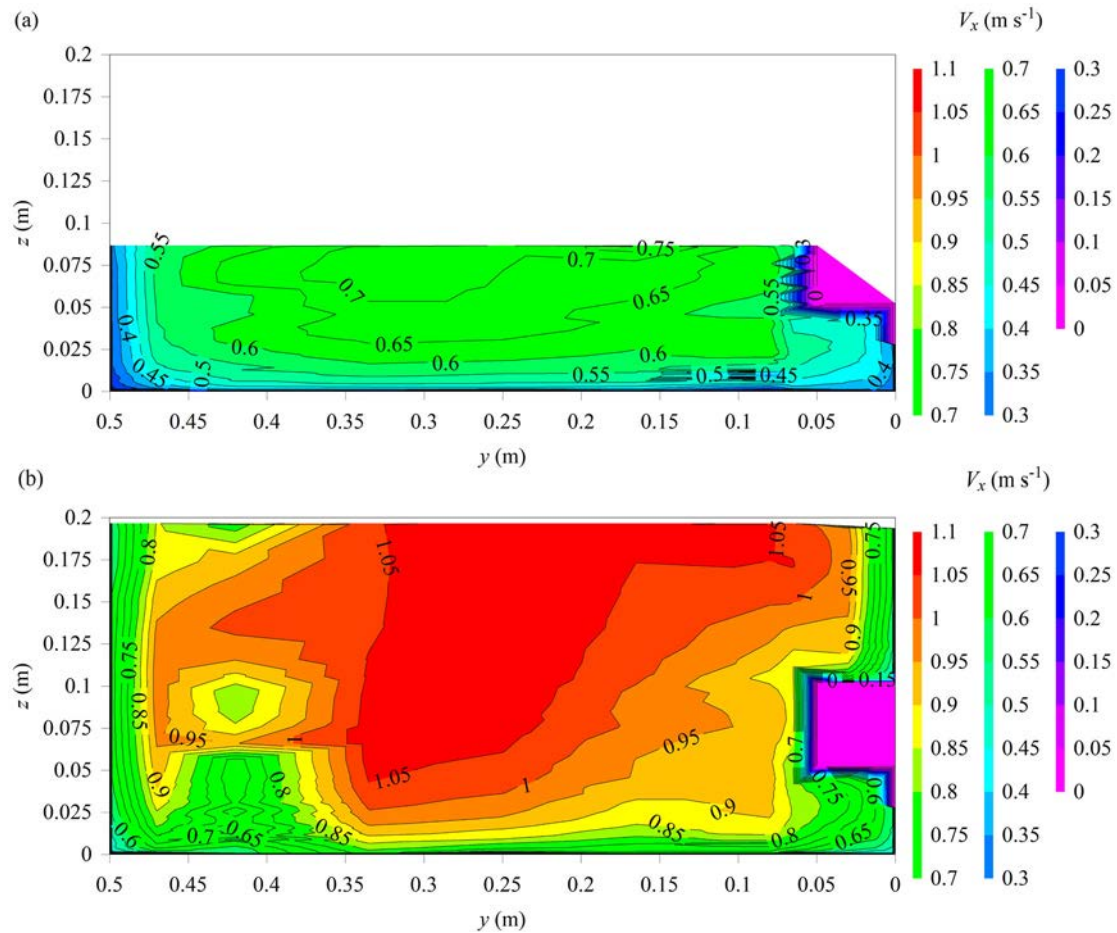


Figure 4 Contour plots of longitudinal velocity component V_x (m/s) in the streamwise ribbed channel looking downstream (streamwise beam on the right of the graphs). (a) $Q = 0.0261$ m³ s⁻¹, $x = 8$ m; (b) $Q = 0.100$ m³ s⁻¹, $x = 8$ m

rib, i.e. for $z < Z_R$ and $y < l_R$. This region was well-defined for all flow conditions, although its surface area was comparatively small.

The vertical profiles of longitudinal velocity showed a phenomenon known as “velocity dip” (Fig. 3). The maximum velocity V_{max} at each transverse location was located below the free surface, and linked to some secondary motion and transverse momentum exchange (Apelt & Xie, 2011). Figure 5 summarizes the experimental observations in the current study.

Maximum velocities were observed to be functions of the transverse location. The largest velocities were about the channel centreline and decreased closer to the sidewalls. The decrease in V_{max}/V_{mean} was more significant with decreasing transverse distance, i.e. towards the ribbed sidewall, highlighting some flow asymmetry. On average, the dimensionless cross-sectional maximum velocity was $(V_{max})_M/V_{mean} \approx 1.14$ observed at about $Z_{V_{max}}/d \approx 0.66$ and $Y_{V_{max}}/B \approx 0.67$. The relative vertical and transversal distance to the maximum velocity was close to

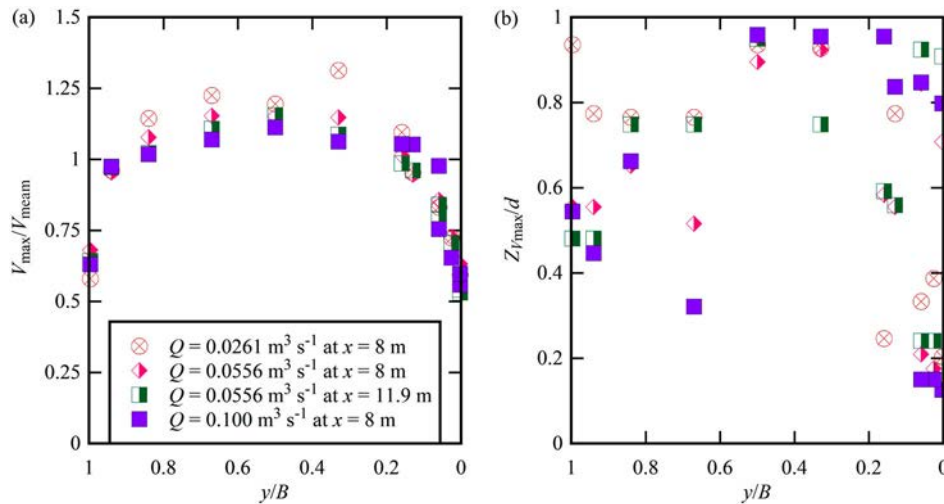


Figure 5 Transverse distribution of maximum longitudinal velocities and corresponding vertical elevations as functions of the transverse distance for the ribbed channel – same legend for both graphs, looking downstream (streamwise beam on the right of the graphs). (a) Maximum velocity V_{max}/V_{mean} ; (b) Elevation to the maximum velocity $Z_{V_{max}}/d$

earlier results in asymmetrical rectangular channels (Table 2). The relative height was also similar to observations in smooth channels: $Z_{V_{max}}/d \approx 0.66$ (Xie, 1998).

The transverse velocities were about zero near the centreline of the flume. Relatively large transverse velocities, up to 0.03 m s^{-1} in magnitude, were observed in the square cavity beneath the rib, as well as next to the rib edges (data not shown). The transverse velocities on the upper external corner of the rib increased with increasing flow rate, and weaker secondary currents were observed beneath the rib at

the largest discharge. The vertical velocity component data presented patterns similar to the transverse velocity data. The findings indicated the presence of strong secondary currents around the rib, extending up to 0.15 m away from the right-hand sidewall. The sharp-edged external and internal corners of the beam played a key role in the development of secondary motion because a transverse flow was directed towards the corner as a direct result of turbulent shear stress gradients normal to the edge bisector (Chanson, 2019; Gessner, 1973; Prandtl, 1952).

Table 2 Experimental flow conditions for velocity measurements in asymmetrical and smooth flumes

Reference	Q ($\text{m}^3 \text{ s}^{-1}$)	B (m)	x (m)	d (m)	V_{mean} (m s^{-1})	Boundary conditions	Instrumentation
Xie (1998)	0.015	0.40	8	0.128	0.2930	Uniform rectangular channel	Laser Doppler velocimetry (LDV), RPT
Cabonce et al. (2019)	0.0261	0.50	8.15	0.096	0.544	Uniform rectangular channel	Prandtl–Pitot tube
Tominaga and Nezu (1991)	0.0556	0.4	7.5	0.162	0.686	0.2 m long 0.005 m high cross-beams	Laser Doppler velocimetry (LDV)
	0.003			0.0392	0.191		
	0.006			0.0603	0.249		
	0.008			0.0603	0.249		
	0.008			0.0795	0.255		
Wang et al. (2018)	0.0261	0.4785	8	0.129	0.423	Rough bed & rough left wall	Prandtl–Pitot tube, ADV
	0.0556			0.1743	0.638		
Cabonce et al. (2019)	0.0261	0.50	8	0.121	0.431	Triangular baffles (left corner)	Prandtl–Pitot tube
	0.1035			0.504			
	0.0556			0.50	0.1625		
Present study	0.0261	0.50	8	0.093	0.589	Streamwise beam (right wall)	Prandtl–Pitot tube, RPT, ADV
	0.0556			0.147	0.783		
	0.100			0.206	0.995		
	0.173			0.643			

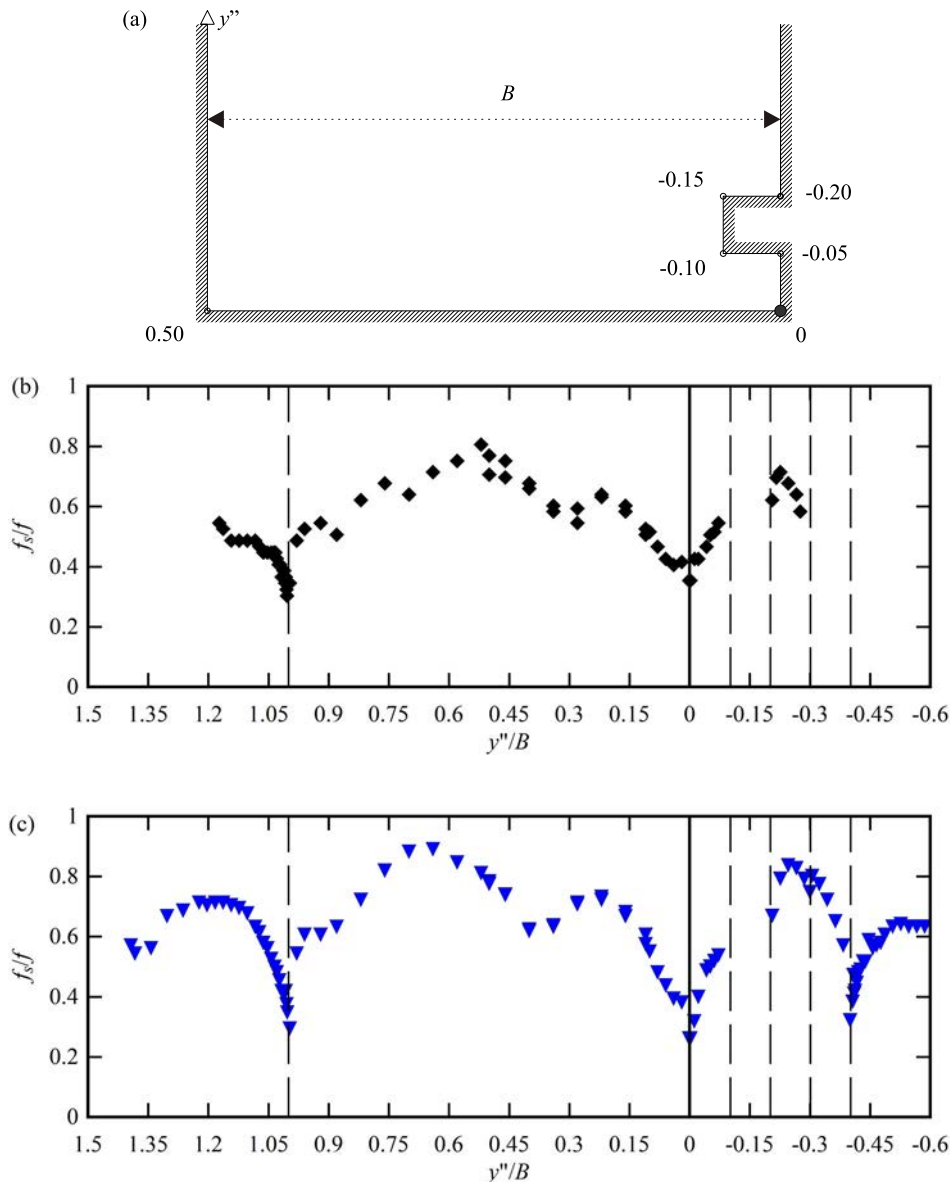


Figure 6 Distributions of dimensionless boundary shear stress f_s/f along the wetted perimeter of the sidewall ribbed channel – vertical black lines represent physical corners (internal or external). (a) Definition sketch of wetted perimeter looking downstream [units: metres]; (b) Regime II, $Q = 0.0261 \text{ m}^3 \text{ s}^{-1}$, $x = 8 \text{ m}$, $f = 0.0248$; (c) Regime III, $Q = 0.100 \text{ m}^3 \text{ s}^{-1}$, $x = 8 \text{ m}$, $f = 0.0148$

4.2 Boundary shear stress distributions

Boundary shear stress measurements were performed along the wetted perimeter, using the Prandtl–Pitot tube and roving Preston tube (RPT). Figure 6 presents typical distributions of dimensionless skin friction boundary shear stress along the wetted perimeter, where f_s is dimensionless skin friction shear stress, f is the dimensionless total boundary shear stress (Section 3.2), and y'' is the wetted perimeter coordinate (Fig. 6a).

The physical data showed a non-uniform distribution of boundary shear stress along the wetted perimeter (Fig. 6). The skin friction boundary shear stress was not symmetrically distributed about the channel centreline. Large boundary shear stresses were recorded along the faces of the sidewall rib, with maximum shear stresses typically observed on the vertical side of the rib and external corners which might be related to local

Table 3 Transverse-averaged skin friction boundary shear stress in the sidewall ribbed channel

Q ($\text{m}^3 \text{ s}^{-1}$)	Regime	x (m)	d (m)	V_{mean} (m s^{-1})	\bar{f}_s	\bar{f}_s/f	Regime
0.0261	II	8	0.093	0.5885	0.0145	0.59	II
0.0556	IIIa	8	0.147	0.7831	0.0098	0.48	IIIa
0.100	IIIb	8	0.206	0.9950	0.0098	0.67	IIIb

Note: Regime: flow regime as defined in Fig. 1.

fluid acceleration and streamwise vorticity. (Note that shear stress measurements could not be conducted along the lower surface of the rib.) Such large skin friction shear stresses might suggest a region of strong interactions between the main flow, secondary currents and cavity recirculation, in a manner similar

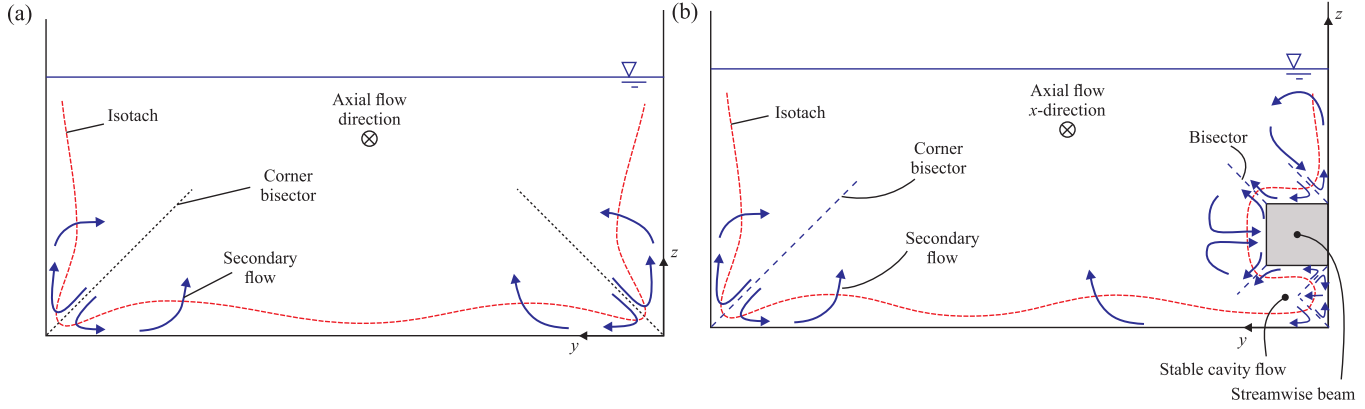


Figure 7 Comparison of secondary circulation in smooth and sidewall ribbed channel, looking downstream. (a) Secondary currents of Prandtl's second kind in a rectangular channel; (b) predicted secondary circulation in a sidewall ribbed channel with sharp corners, looking downstream – undistorted sketch for $Q = 0.100 \text{ m}^3 \text{ s}^{-1}$

to observations on heterogeneous transverse roughness (Tomimaga & Nezu, 1991). Minimum shear stresses were typically observed on the bottom inner corners of the flume, as predicted theoretically (Liggett, Chiu, & Miao, 1965). The large perimetric gradients $\partial\tau_o/\partial y''$ in boundary shear stress were clear evidence of large secondary flow cells in the canal with streamwise beam (Macintosh, 1990; Shiono & Knight, 1991).

Along the flume bottom, the boundary shear stress data presented a transverse shape with two dips, observed about $y/B \approx 0.4$ and 0.85 . The bottom profile implied the existence of two large longitudinal vortical structures in the main flow region, plus one longitudinal structure in the cavity beneath the rib. Minimum shear stresses were typically observed on the bottom corners of the flume. The present data showed that the local skin friction boundary shear stress was consistently less than the total boundary shear stress, i.e. $f_s/f < 1$ (Fig. 6). The average dimensionless boundary shear stress appeared to be little affected by the Reynolds number, but the transverse distribution shape changed in response to different rib submergence ratio and flow regime.

The boundary shear stress data were integrated along the wetted perimeter, yielding the cross-sectional averaged skin friction boundary shear stress:

$$\bar{\tau}_o = \frac{1}{P_w} \int_{P_w} \tau_o dy'' \quad (3)$$

where P_w is the wetted perimeter. The data are summarized in Table 3 in dimensionless form. Depending upon the flow conditions, the ratio of mean skin friction resistance to total flow resistance \bar{f}_s/f ranged from 0.48 to 0.67. The lowest ratio was observed in Regime III, when a strong secondary motion was observed below, above and beside the sidewall rib.

5 Discussion

In a smooth rectangular channel, secondary flows originate at the channel boundaries and streamwise corners because of

turbulence anisotropy. They are referred to as secondary currents of Prandtl's second kind (Prandtl, 1952). Secondary flows are directed at a right angle to the main stream direction and redistribute momentum across the channel (Naot & Rodi, 1982; Perkins, 1970). In a streamwise corner, the interactions between the transverse shear gradient along the corner bisector and longitudinal flow motion induce energy losses, which must be compensated by some transverse flow, bringing a net influx of energy in control volumes along the corner bisector (Gessner, 1973) (Fig. 7a).

The production of turbulence-induced secondary currents in a prismatic open channel flow may be explained by the longitudinal vorticity equation (Tomimaga, Nezu, Ezaki, & Nakagawa, 1989). The longitudinal vorticity equation in fully-developed turbulent flow is given as (Gerard, 1978):

$$V_z \frac{\partial \omega_x}{\partial z} + V_y \frac{\partial \omega_x}{\partial y} = \frac{\partial^2}{\partial z \partial y} (v_z^2 - v_y^2) + \left(\frac{\partial^2}{\partial y^2} - \frac{\partial^2}{\partial z^2} \right) \overline{v_y v_z} + \frac{\mu}{\rho} \left(\frac{\partial^2 \omega_x}{\partial z^2} + \frac{\partial^2 \omega_x}{\partial y^2} \right) \quad (4)$$

where ω_x is the vorticity component in the x -direction:

$$\omega_x = \frac{\partial V_y}{\partial z} - \frac{\partial V_z}{\partial y} \quad (5)$$

In Eq. (4), the first term on the right-hand side is the vorticity production terms, and the last term is a viscous term, often neglected except very close to the wall. After rearrangement, one found that the structure of the secondary current is determined by the distribution of $(v_y^2 - v_z^2)$ (Gerard, 1978; Tomimaga et al., 1989). The transverse distribution of the difference of normal stresses $(v_y^2 - v_z^2)$ plays an essential role (Perkins, 1970). When the convection and diffusion terms are small compared to the production term, Eq. (4) may reduce to (Gerard, 1978):

$$\frac{\partial^2}{\partial z \partial y} (v_z^2 - v_y^2) + \left(\frac{\partial^2}{\partial y^2} - \frac{\partial^2}{\partial z^2} \right) \overline{v_y v_z} = 0 \quad (6)$$

Secondary currents develop spontaneously in turbulent flows, particularly when the term $(v_y^2 - v_z^2)$ has values different from zero. In an open channel, unstable and instantaneous secondary currents are present in the form of longitudinal vortices (Jackson, 1976; Nezu, 2005). More stable secondary motion may be generated in cavity flow, as sketched in Fig. 7b. In turn, a prediction of secondary motion in a sidewall beam canal may be derived based upon basic turbulence theoretical considerations (Gessner, 1973; Montes, 1998; Naot & Rodi, 1982). When a lateral variation of near-wall velocity/boundary shear stress exists, secondary flows are induced and non-uniform distribution of boundary shear stress may be observed.

The development of secondary flows and their scale essentially depends upon the corner configuration geometry, while the direction of the secondary motion remains predominantly in the transverse plane. With a sidewall streamwise beam, the geometry adds two inner and two outer corners to the channel cross-section. Secondary circulation of Prandtl's second kind may be found in the flow cross-section linked to the abrupt spatial variations in boundary conditions, i.e. sharp corners between bed and sidewall, along the sidewall rib, and between sidewall and free-surface. One sees that the ribbed configuration may be conducive to the development of strong secondary currents, sketched in Fig. 7b, associated with high-turbulence low-velocity regions beneath and above the sidewall rib. An obvious effect of the secondary motion is that it greatly alters the main velocity field, while promoting the transverse convection of streamwise momentum.

6 Conclusion

The turbulent losses in a sidewall longitudinal beam canal were essentially regular losses, albeit with a complicated turbulent flow field and intense secondary currents. The flow pattern resulted in regions of contrasted longitudinal velocities, i.e. high and low velocity regions, with the lowest velocities typically recorded underneath the sidewall beam. The sidewall rib, its streamwise corners and the channel asymmetry contributed to some strong secondary motion, associated with turbulent dissipation. Complicated secondary currents of Prandtl's second kind developed, in particular in the square cavity, linked to low-velocity and high-turbulence. A key feature of the channel design was the provision of a well-marked high-turbulence low velocity region beneath the sidewall rib, for all tested flow conditions.

Altogether this detailed investigation demonstrated how the introduction of a relatively simple streamwise shape (i.e. square rib) may yield a major change in hydrodynamic properties, in comparison to a smooth symmetrical rectangular channel flow. The current hydrodynamic study showed unequivocally that the flow in an asymmetrical ribbed channel is extremely complicated, while the design presents a number of manufacturing,

installation and operational issues, including very high risks of blockage by sediments and debris, that must be taken into account before the final design selection. Such practical considerations have direct implications in the suitability of such designs in sanitary engineering, water treatment and biological applications (e.g. fish passage).

Acknowledgements

The authors thank Dr John Macintosh (Water Solutions, Australia), Professor Oscar Castro-Orgaz (University of Cordoba, Spain), and Professor Benoit Cushman-Roisin (Dartmouth College, USA) for their very valuable comments. They further thank Professor Donald Knight (University of Birmingham, UK) for helpful advice. The authors acknowledge the assistance of Ms Matilda Meppem during some experiments. They acknowledge the technical assistance of Jason Van Der Gevel and Stewart Matthews (The University of Queensland). The financial support through the Australian Research Council (Grant LP140100225) is acknowledged. Hubert Chanson has competing interest and conflict of interest with Craig E. Franklin.

Funding

The financial support through the Australian Research Council (Grant LP140100225) is acknowledged.

Supplemental data

Supplemental materials including tabular data are presented in Sanchez et al. (2018) and can be accessed online at {<https://espace.library.uq.edu.au/view/UQ:0b74ff5>}.

Notation

A	= channel cross-section area (m ²)
B	= channel width (m): $B = 0.5$ m in the present study
b	= free-surface width (m)
$C_{\text{Chézy}}$	= Chézy coefficient (m ^{1/2} s ⁻¹)
D_H	= hydraulic diameter (m): $D_H = 4A/P_w$
d	= water depth (m)
d_c	= critical flow depth (m)
d_1	= inflow depth (m)
f	= Darcy–Weisbach friction factor (–)
f_s	= skin friction factor measured with a Prandtl–Pitot/RPT tube lying on the bed (–)
\bar{f}_s	= cross-section-averaged skin friction factor (–)

f_{KN}	= friction factor for smooth turbulent flows (Karman–Nikuradse formula) (–)
g	= gravity acceleration (m s^{-2}): $g = 9.794 \text{ m s}^{-2}$ in Brisbane, Australia
h_R	= height of longitudinal rib (m)
k_s	= equivalent sand roughness height (m)
l_R	= breadth of longitudinal rib (m)
n_{GM}	= Gauckler–Manning coefficient for flow resistance in open channel ($\text{s m}^{-1/3}$)
P	= pressure (Pa)
P_w	= wetted perimeter (m)
Q	= water discharge ($\text{m}^3 \text{ s}^{-1}$)
q	= unit discharge ($\text{m}^2 \text{ s}^{-1}$)
Re	= Reynolds number defined in terms of the hydraulic diameter (–)
r_R	= radius of curvature of longitudinal rib edges (m)
S_o	= bed slope: $S_o = \sin\theta$ (–)
V	= velocity (m s^{-1})
V_c	= critical flow velocity (m s^{-1})
V_{\max}	= maximum velocity (m s^{-1})
V_{mean}	= cross-sectional mean velocity (m s^{-1}): $V_{\text{mean}} = Q/A$
V_1	= inflow velocity (m s^{-1})
v'	= velocity fluctuation (m s^{-1})
x	= longitudinal distance (positive downstream) (m)
$Y_{V_{\max}}$	= transverse distance where $V_x = (V_{\max})_M$ (m)
y	= transverse distance measured from the right sidewall positive towards the left sidewall (m)
y''	= transverse coordinate following the wetted perimeter, with $y'' = 0$ at the bottom right corner (m)
Z_R	= vertical elevation of longitudinal rib bottom above the channel bed (m)
$Z_{V_{\max}}$	= vertical elevation where $V_x = V_{\max}$ (m)
z	= vertical distance positive upwards with $z = 0$ at the invert (m)
μ	= dynamic viscosity of water (Pa s)
ω	= vorticity (s^{-1})
θ	= angle between bed slope and horizontal ($^\circ$)
ρ	= water density (kg m^{-3})
σ	= surface tension between air and water (N m^{-1})
τ	= Reynolds shear stress (Pa)
τ_o	= boundary shear stress (Pa)
$\bar{\tau}_o$	= cross-sectional averaged boundary shear stress (Pa)
\emptyset	= diameter (m)

Subscript

c	= critical flow conditions
M	= cross-sectional maximum value
R	= rib characteristics
x	= longitudinal component

y	= transverse component
z	= vertical component
1	= upstream flow conditions

ORCID

Xinqian Leng  <http://orcid.org/0000-0001-8472-7925>

Hubert Chanson  <http://orcid.org/0000-0002-2016-9650>

References

- Adachi, S. (1964). On the artificial strip roughness. *Disaster Prevention Research Institute Bulletin No.69*, Kyoto University, Japan, 20 pages.
- Apelt, C. G., & Xie, Q. (2011). Measurements of the turbulent velocity field in a non-uniform open channel. *Proc. 34th IAHR World Congress*, Brisbane, Australia, 26 June-1 July, Engineers Australia Publication, Eric Valentine, Colin Apelt, James Ball, Hubert Chanson, Ron Cox, Rob Ettema, George Kuczera, Martin Lambert, Bruce Melville and Jane Sargison Editors, 3338–3345.
- British Standard. (1943). *Flow measurement*. British Standard Code BS 1042:1943. London: British Standard Institution.
- Cabonco, J., Fernando, R., Wang, H., & Chanson, H. (2019). Using small triangular baffles to facilitate upstream fish passage in standard box culverts. *Environmental Fluid Mechanics*, 19, 157–179. doi:10.1007/s10652-018-9604-x (In print)
- Chang, S. W., Lin, C. C., & Liou, J. S. (2008). Heat transfer in a reciprocating curved square duct fitted with longitudinal ribs. *International Journal of Thermal Sciences*, 47, 52–67.
- Chanson, H. (2014). *Applied hydrodynamics: An introduction*. CRC Press, Taylor & Francis Group, Leiden, The Netherlands, 448 pages & 21 video movies.
- Chanson, H. (2019). Utilising the boundary layer to help restore the connectivity of fish habitats and populations. An engineering discussion. *Ecological Engineering*, 141, 105613, 5 pages. doi:10.1016/j.ecoleng.2019.105613
- Chanson, H., Trevethan, M., & Aoki, S. (2008). Acoustic doppler velocimetry (ADV) in small estuary: Field experience and signal post-processing. *Flow Measurement and Instrumentation*, 19(5), 307–313. doi:10.1016/j.flowmeasinst.2008.03.003
- Degremont. (1979). *Water treatment handbook* (5th ed.). New York, NY: Halsted Press Book, John Wiley & Sons.
- Djenidi, L., Elavarasan, R., & Antonia, R. A. (1999). The turbulent boundary layer over transverse square cavities. *Journal of Fluid Mechanics*, 395, 271–294.
- FNDAE. (1988). Les Bassins d’Orage sur les Réseaux d’Assinissement. *Documentation technique No. 6*, Fonds National pour le Développement des Adductions d’eau, Ministère de l’Agriculture, Paris, France, 61 pages (in French).

- Gerard, R. (1978). Secondary flow in noncircular conduits. *Journal of Hydraulic Division, ASCE*, 104(HY5), 755–773.
- Gessner, F. B. (1973). The origin of secondary flow in turbulent flow along a corner. *Journal of Fluid Mechanics*, 58(1), 1–25.
- Goring, D. G., & Nikora, V. I. (2002). Despiking acoustic Doppler Velocimeter data. *Journal of Hydraulic Engineering, ASCE*, 128(1), 117–126.
- Hwang, H. G., & Lee, J. H. (2018). Secondary flows in turbulent boundary layers over longitudinal surface roughness. *Physical Review Fluids*, 3, Paper 014608. doi:10.1103/PhysRevFluids.3.014608
- Jackson, R. G. (1976). Sedimentological and fluid-dynamic implications of the turbulent bursting phenomenon in geophysical flows. *Journal of Fluid Mechanics*, 77(3), 531–560.
- Knight, D. W., & Macdonald, J. A. (1979). Hydraulic resistance of artificial strip roughness. *Journal of Hydraulic Division, ASCE*, 105(HY6), 675–690.
- Liggett, J. A. (1994). *Fluid mechanics*. New York, NY: McGraw-Hill.
- Liggett, J. A., Chiu, C. L., & Miao, L. S. (1965). Secondary currents in a corner. *Journal of Hydraulic Division, ASCE*, 91(HY6), 99–117.
- Macintosh, J. C. (1990). Hydraulic characteristics in channels of complex cross-section. Ph.D. thesis. University of Queensland, Department of Civil Engineering, Australia, November, 487 pages. doi:10.14264/uql.2015.218
- Montes, J. S. (1998). *Hydraulics of open channel flow*. New York, NY: ASCE Press, 697 pages.
- Morris, H. M. (1955). A new concept of flow in rough conduits. *Transactions, ASCE*, 120, 373–410.
- Naik, S., Probert, S. D., & Bryden, I. G. (1999). Heat transfer characteristics of shrouded longitudinal ribs in turbulent forced convection. *International Journal of Heat and Mass Transfer*, 20, 374–384.
- Naot, D., & Rodi, W. (1982). Calculation of secondary currents in channel flow. *Journal of Hydraulic Division, ASCE*, 108(HY8), 948–967.
- Nezu, I. (2005). Open-channel flow turbulence and its research prospect in the 21st century. *Journal of Hydraulic Engineering, ASCE*, 131(4), 229–246.
- Patel, V. C. (1965). Calibration of the Preston Tube and limitations on its use in pressure gradients. *Journal of Fluid Mechanics*, 23(1), 185–208.
- Perkins, H. J. (1970). The formation of streamwise vorticity in turbulent flow. *Journal of Fluid Mechanics*, 44(4), 721–740.
- Prandtl, L. (1952). *Essentials of fluid dynamics with applications to hydraulics, aeronautics, meteorology and other subjects*. London, UK: Blackie & Son. 452 pages.
- Preston, J. H. (1954). The determination of turbulent skin friction by means of pitot tubes. *Journal of Royal Aeronautical Society, London*, 58, 109–121.
- Randtke, S. J., & Horsley, M. B. (2012). *Water treatment plant design* (5th ed.). New York: McGraw-Hill, American Water Works Association and American Society of Civil Engineers.
- Roo, J. T. (1965). Horizontal filter structure. *US Patent 3,216,576*, Publication US3216576A, 4 pages & 4 plates.
- Rouse, H. (1938). *Fluid mechanics for hydraulic engineers*. New York: McGraw-Hill, 422 pages.
- Sanchez, P. X., Leng, X., & Chanson, H. (2018). *Fluid dynamics and secondary currents in an asymmetrical rectangular canal with sidewall streamwise rib*. Hydraulic Model Report No. CH113/18. School of Civil Engineering, The University of Queensland, Brisbane, Australia, 158 pages.
- Schlichting, H. (1979). *Boundary layer theory* (7th ed.). New York, NY: McGraw-Hill.
- Shiono, K., & Knight, D. W. (1991). Turbulent open-channel flows with variable depth across the channel. *Journal of Fluid Mechanics*, 222, 617–646. (& 231, 693).
- Stamou, A. (2008). Improving the hydraulic efficiency of water process tanks using CFD models. *Chemical Engineering and Processing: Process Intensification*, 47, 1179–1189.
- Tominaga, A., & Nezu, I. (1991). Turbulent structure of shear flow with spanwise roughness heterogeneity. In *Proc. International Symposium on Environmental Hydraulics*, Hong Kong, 16–18 Dec., (pp. 415–420). Rotterdam: Balkema Publ.
- Tominaga, A., Nezu, I., Ezaki, K., & Nakagawa, H. (1989). Three-dimensional turbulent structure in straight open channel flows. *Journal of Hydraulic Research, IAHR*, 27(1), 149–173.
- Vanderwel, C., & Ganapathisubramani, B. (2015). Effects of spanwise spacing on large-scale secondary flows in rough-wall turbulent boundary layers. *Journal of Fluid Mechanics*, 771(R2), 12 pages. doi:10.1017/jfm.2015.292
- Wahl, T. L. (2003). Discussion of “Despiking acoustic Doppler Velocimeter data” by Derek G. Goring and Vladimir I. Nikora. *Journal of Hydraulic Engineering, ASCE*, 129(6), 484–487.
- Wang, H., Uys, W., & Chanson, H. (2018). Alternative mitigation measures for fish passage in standard box culverts: Physical modelling. *Journal of Hydro-environment Research, IAHR*, 19, 214–223. doi:10.1016/j.jher.2017.03.001
- Watson, J., Goodrich, H., Cramp, R., Gordos, M., & Franklin, C. (2018). Utilising the boundary layer to help restore the connectivity of fish habitats and populations. *Ecological Engineering*, 122, 286–294.
- Xie, Q. (1998). Turbulent flows in non-uniform open channels: Experimental measurements and numerical modelling. Ph.D. thesis, Dept. of Civil Eng., University Of Queensland, Australia, 339 pages.

Appendix 1

First developed by Jean-Baptiste Bélanger, the notion of critical flow conditions was associated to the minimum in specific energy by Boris A. Bakhmeteff. For an irregular channel, the flow conditions at minimum specific energy equation, i.e. critical flow conditions, satisfy:

$$1 - \frac{Q^2}{g(A^3/b)} = 0 \tag{A1}$$

with Q the discharge, g the gravity acceleration, A the flow cross-section area and b the free-surface width (Fig. 1).

For a steady turbulent flow in the asymmetrical rectangular channel sketched in Fig. 1, the free-surface width, flow cross-section area, hydraulic diameter and critical depth are functions of the flow regimes sketched in Fig. 1. The analytical solutions are presented in Table A1.

Table A1 Free-surface width, cross-section area, wetted perimeter and critical depth in an asymmetrical rectangular channel with streamwise beam (Fig. 1)

	Regime I		Regime II	Regime III
Free-surface width b	B	$B - l_R$		B
Cross-section area A	$B \times d$	$Bd - (d - Z_R)l_R$		$Bd - h_R l_R$
Wetted perimeter P_w	$B + 2 \times d$	$B + d + Z_R + l_R + (d - Z_R)$		$B + d + Z_R + 2 \times l_R + h_R + (d - (Z_R + h_R))$
Critical depth d_c	$\sqrt[3]{Q^2/g B^2}$	$\frac{1}{1 - l_R/B} \left(\sqrt[3]{(1 - l_R/B)Q^2/g B^2} - Z_R l_R/B \right)$		$h_R l_R/B + \sqrt[3]{Q^2/g B^2}$